TOPICAL COLLECTION: ADVANCED METAL ION BATTERIES

Improved Lithium Storage Capability of Si Anode by Ball-Milling Produced Graphitic Carbon Sheet and Fe_3O_4 Nanoparticles

Junkai Ma[1] · Yuxuan Zheng[1] · Yongping Gan[1] · Jun Zhang[1] · Yang Xia[1] · Xinping He[1] · Wenkui Zhang[1] · Hui Huang[1]

Abstract

Silicon is considered the most promising material for anodes for the development of lithium-ion batteries (LIBs) due to its high theoretical capacity and natural abundance. However, the poor intrinsic conductivity and serious volume changes severely restrain the practical application. To address these issues, combining Si with carbon is confirmed as an effective strategy, but still suffers from uneven combination, poor interfacial contact and inferior electrochemical performance. Herein, Si@Fe_3O_4@C composites were synthesized by facile scalable ball-milling of nanosilicon, mesophase carbon microspheres (MCMB) and iron scurf from a stainless steel reactor. As compared to Si/C, the Si@Fe_3O_4@C composites exhibit much improved specific capacity, cycling stability and rate performance. The Fe_3O_4 nanoparticles not only help to boost the conductivity of Si but also accommodate their volume expansion during cycling. Consequently, the Si@Fe_3O_4@C anode delivers a reversible capacity of 1009 mA h g^{-1} at 200 mA g^{-1} after 110 cycles and 780.8 mA h g^{-1} at 1 A g^{-1} after 500 cycles. The method shows the merits of low cost, facile operation and easy industrial production for the synthesis of high-capacity Si anodes.

Introduction

Over the past several years, many novel materials have been explored to meet the growing demands of high energy-density lithium-ion batteries (LIBs).[1–4] The Si-based anode is considered one of the most promising candidates because of a high theoretical capacity of 4200 m A h g^{-1} and a de-intercalation potential lower than 0.5 V versus Li/Li^{+}. However, the huge volume expansion of Si during the lithiation process leads to particle pulverization, unstable solid-electrolyte interface (SEI) layer growth, and delamination of active components, which severely deteriorates its lithium storage capability and limits the further practical applications of Si-based materials.[5–8]

To solve these issues, the rational design of a Si/C composite is confirmed to effectively improve the electrochemical performance.[9–12] Ball milling is an attractive route for industrial production of the Si/C composite due to its simple operation and high efficiency. However, it still suffers from weak interface bonding, uneven dispersion, and poor interfacial contact of Si and C components.[13–16] Therefore, it is particularly important to seek a new component that enhances the overall stability of the Si/C composite.[17,18] Iron oxides (Fe_3O_4, Fe_2O_3) show high theoretical capacity, good safety and low price as anode materials for LIBs.[19–22] It was found that iron oxides can effectively alleviate the structural rupture, promote the formation of a stable SEI film, improve the electrical conductivity, and thus greatly enhance the cycling stability of the Si-based electrode.[23,24] For example, Grinbom et al.[25] reported that Fe_2O_3 coating promotes the formation of a thick SEI film on the Si surface, leading to the improvement of the rate capability and lithium storage performance. Liao et al.[26] found that Fe_3O_4 is in situ reduced to Fe (0) nanocrystals during lithiation, which can accelerate the dynamic diffusion of Li^{+} and improve pseudocapacitive behavior. Moreover, Su et al.[27] further revealed that Fe (0) is chemically active and acts as an electrocatalyst to promote the reversible transformation of some SEI components (especially Li_2CO_3). So, it is inferred that iron oxide is effective in promoting the electrochemical

✉ Hui Huang
hhui@zjut.edu.cn

[1] College of Materials Science and Engineering, Zhejiang University of Technology, Hangzhou 310014, People's Republic of China

kinetics of the Si/C composite. Liu et al. synthesized a Si@Fe_3O_4@FLG core-shell structure by one-step ball milling with K_2FeO_4 as the iron source. Fe_3O_4 as a silicon-carbon interlayer effectively relieved the volume expansion of Si, enabling 1600 long cycles at 2 A g^{-1}.[28] Wang et al.[29] introduced Fe from stainless steel by ball milling, and the Fe_3O_4-containing Si@GC composite provided a specific capacity of 1450.7 mA h g^{-1} after 400 cycles at 0.5 A g^{-1}.

In this study, Si@Fe_3O_4@C composites were synthesized from commercial nanosized Si powder and mesophase carbon microspheres (MCMB) by wet ball milling and subsequent heat treatment, where MCMB is stripped into two-dimensional graphite sheets under strong shear stress, which are expected to buffer the volume expansion of Si during the lithium process and improve the electronic/ionic conductivity of the composite.[30,31] Fe_3O_4 not only provides part of the capacity, but also plays a role in stabilizing the SEI film. As a result, the Si@Fe_3O_4@C composite shows high capacity and excellent rate capability and cycling stability. Notably, such a facile, scalable route provides a great chance for practical applications because it possesses merits of large-scale capability, environmental benignity, and low cost.

Experimental Section

Material Synthesis

The nanosized Si powder and MCMB were ultrasonically pre-dispersed in 30 mL solution $(CH_2OH)_2$: C_2H_5OH=2:1, v/v) at a mass ratio of 1:4 and then transferred to a stainless steel jar. The ball milling was conducted in a planetary ball mill (QM-3SP4, Nanjing) at a speed of 300 r min^{-1} for 12 h. Afterwards, it was washed several times with absolute ethanol and deionized water, and the Si@Fe_3O_4@C precursor was collected by freeze-drying. Finally, Si@Fe_3O_4@C was obtained by annealing at 550°C for 3 h under inert Ar atmosphere. For comparison, the Si@C composite was prepared by a similar process in the ZrO_2 ball-milling jars.

Materials Characterization

X-ray diffraction (XRD) analysis was carried out on an X'Pert Pro diffractometer using copper Kα radiation (λ = 1.5418 Å). The chemical state of the samples was investigated by x-ray photoelectron spectroscopy (XPS; Thermo Scientific K-Alpha) with a Al Kα source gun at 1486.6 eV. The Raman spectra were recorded with an excitation wavelength of 532 nm using a Renishaw InVia Reflex spectrometer. The morphology of the electrodes was characterized using an FEI Nova NanoSEM 450 scanning electron microscope (SEM) operated at 15.0 kV and an FEI Tecnai G2 F30

transmission electron microscope (TEM) equipped with an energy-dispersive spectrometer (EDS) operated at 300 kV.

Electrochemical Measurements

The electrochemical performance of the composites was tested by assembling a CR2032-type coin cell in an argon-filled glove box (O_2 < 0.1 ppm, H_2O < 0.1 ppm), with a Cellgard 2500 film as a separator, a lithium foil as the counter electrode, and 1M $LiPF_6$ in an equal volume solution of ethylene carbonate (EC), diethyl carbonate (DEC) and dimethyl carbonate (DMC) as the electrolyte. A mixture of active material, super P and polyacrylic acid (PAA) with a mass ratio of 6:2:2 was uniformly coated on the copper sheet, then dried in a vacuum oven at 100°C for 12 h, and cold-pressed under a pressure of 15 MPa to form a working electrode, the average mass loading of the electrode is 1.2 mg cm^{-2}. Cyclic voltammetry tests were conducted on a CHI660E electrochemical workstation with a scan rate of 0.1 mV s^{-1} and a voltage range of 0.01 V~3 V. Electrochemical impedance spectroscopy (EIS) was performed on a Zahner Zennium workstation with a frequency range of 1 MHz to 0.1 Hz. Galvanostatic charge and discharge tests adopts a CT-3008W Neware battery test system, and the test voltage ranges are 0.01 V~3 V and 0.01 V~1.5 V, respectively.

Results and Discussion

The schematic illustration of synthesis of the Si@Fe_3O_4@C composite is shown in Fig. 1. Here, MCMB was employed as the carbon source for preparing the Si/C composite. As we know, MCMB is a micron-grade spherical carbon material with layered stacking structure, generated by thermal condensation of heavy aromatic compounds such as asphalt. Currently, MCMB has been extensively used as anode material for commercial LIBs due to good lithium-ion diffusion, mechanical stability and electrical conductivity. During the ball-milling process, MCMB was broken into graphite flakes under strong shear stress and Fe powder resulted from the grinding of stainless steel jars is oxidized into Fe ions. The as-milled mixture was further calcined under Ar atmosphere. At this stage, Fe_3O_4 undergoes crystallization reaction to obtain Si@Fe_3O_4@C composites.

The XRD pattern of the as-milled sample is shown in Figure S1 to reveal pristine phases. In addition to MCMB, Si raw materials, the stainless steel phase is detected, which results from the grinding of ball mill gar. The XPS spectrum of Si@Fe_3O_4@C precursor (Figure S2) reveals the presence of Fe–O bonds, Fe^{2+} and Fe^{3+}, indicating that amorphous Fe_3O_4 may be formed during milling in the alcoholic solution.[26] In the subsequent calcination procedure, Fe_3O_4 undergoes a structural transformation from amorphous to
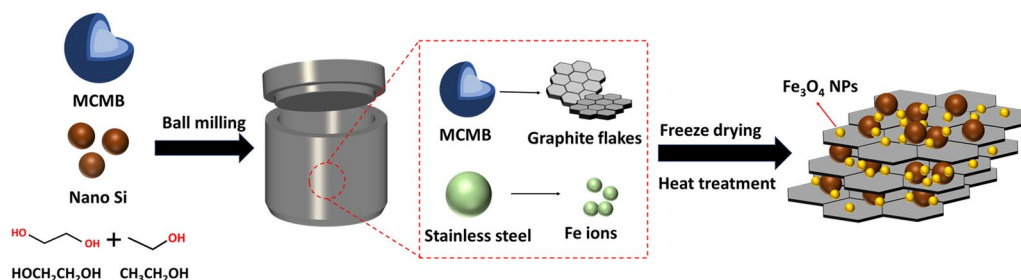
Fig. 1 Schematic illustration of Si@Fe₃O₄@C synthesis by ball milling.

crystalline state. As shown in Fig. 2a, the diffraction peaks of Fe₃O₄ phase are observed in the XRD pattern of Si@Fe₃O₄@C. By comparison, the sample prepared in the zirconia ball mill jar only contains Si and C, no Fe₃O₄ phase is found. The Raman spectra of Si@Fe₃O₄@C are shown in Fig. 2b. The peaks located at 505 cm⁻¹ and 932 cm⁻¹ correspond to crystalline Si. Two other weak peaks at 1340 cm⁻¹ and 1578 cm⁻¹ are assigned to the *D* and *G* bands of carbon, representing the lattice defect of carbon atoms and sp²-hybridized crystalline graphitized carbon, respectively. The peak intensity ratio (I_D/I_G) reveals the graphitization degree of carbon materials.[32] The I_D/I_G of Si@Fe₃O₄@C and MCMB raw material were 0.81 and 0.51, respectively. The higher ratio of Si@Fe₃O₄@C indicates that the milling of spherical MCMB into flakes slightly increases the disorder degree and defects of graphic carbon, resulting in more lithium storage sites.[33]

An XPS survey was employed to show the elementary composition and chemical states of the Si@Fe₃O₄@C composite. The overall XPS survey confirms the presence of Si, C, O, Fe, Mn and Cr (Fig. 3a). Obviously, Mn and Cr originated from the grinding of stainless steel gars/beads. The Si 2p spectra (Fig. 3b) presents

three peaks at 99.7, 100.3 and 102.8 eV, corresponding to two chemical states. Si 2p₃/₂ (99.7 eV) and Si 2p₁/₂ (100.3 eV) represent different p orbitals of pure Si, and the peak located at 102.8 eV can be fitted to Si–O bonds, which is due to the oxidation of Si during the ball-milling process. The formation of a silicon-oxygen layer on the surface of Si can limit the volume expansion during lithium intercalation.[34] According to the high-resolution spectrum of Fe 2p (Fig. 3c), the peaks at 711 and 724.7 eV can be ascribed to the Fe⁺²2p₁/₂ and Fe⁺²2p₃/₂ states, while the peaks at 713 and 726.6 eV correspond to the Fe⁺³2p₁/₂, and Fe⁺³2p₃/₂ states, respectively. The XPS result of Fe 2p is in agreement with previously reported values for Fe₃O₄.[35] The C1s spectrum (Fig. 3d) indicates the presence of C–C, C–O and O–C=O in the composites.[36,37] The presence of Si–O and C–O can be attributed to the oxidation process carried in the solvent ethylene glycol.

To further characterize the morphology and microstructure of the Si@Fe₃O₄@C composite, the samples were subjected to SEM (Figure S3) and TEM analysis. As shown in Fig. 4a and b and Figure S3a, after experiencing huge shear stress, spherical particles of MCMB were exfoliated into graphitic carbon sheets. Figure 4c marks the lattice fringes
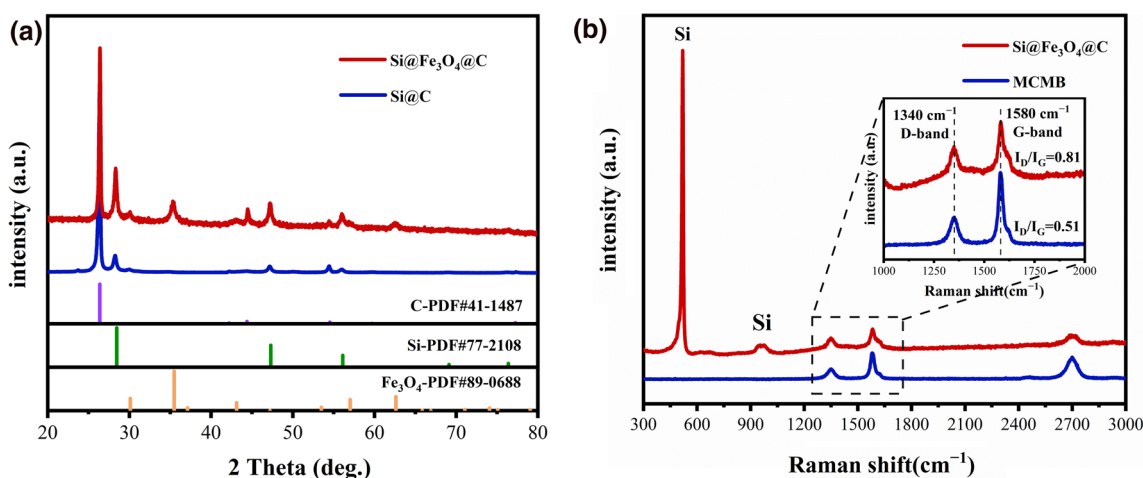

Fig. 2 (a) XRD patterns of Si@C and Si@ Fe₃O₄@C composite, (b) Raman spectra of Si@ Fe₃O₄@C composite and MCMB.
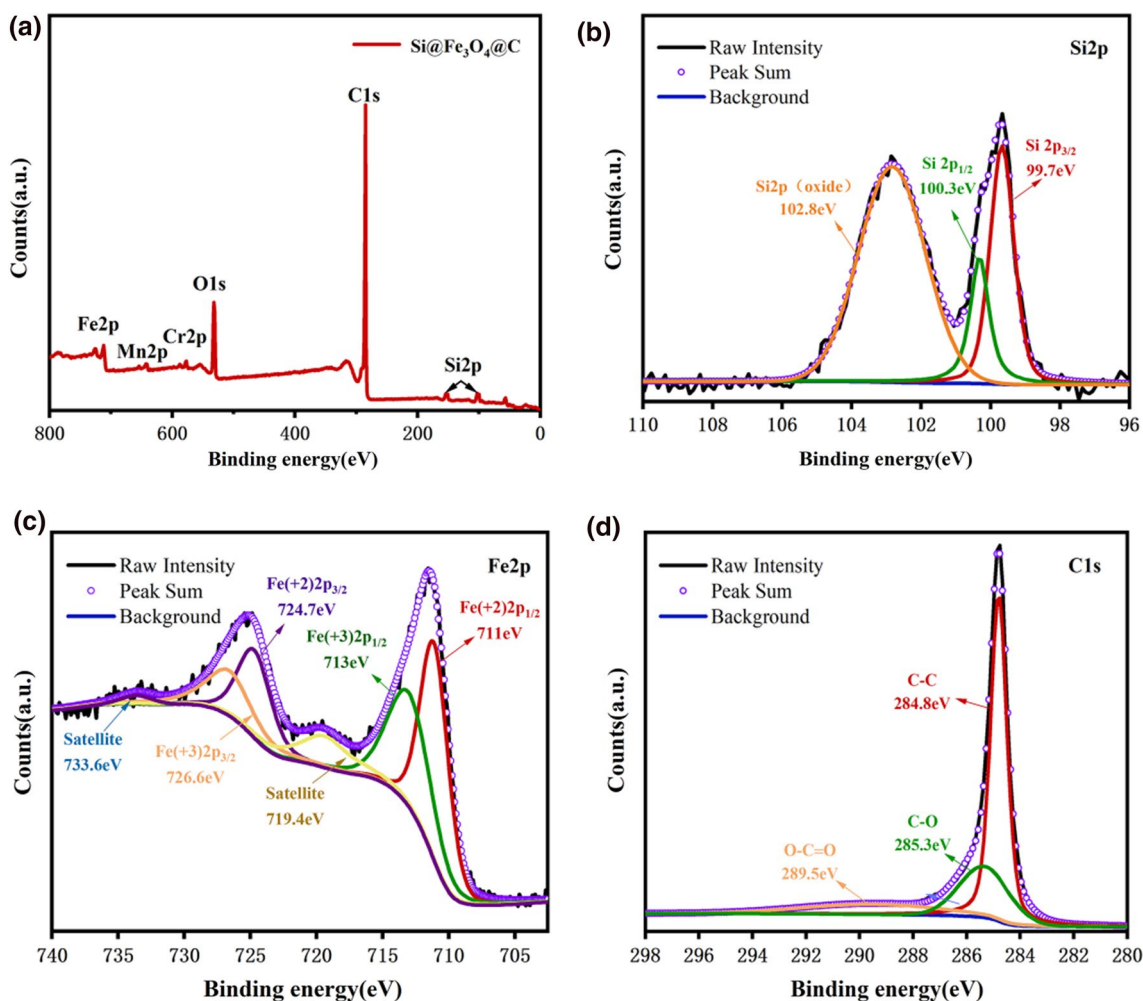
Fig. 3 (a) XPS survey and fine scan XPS spectra of (b) Si 2p, (c) Fe 2p, and (d) C 1s for the Si@Fe_3O_4@C composite.

of graphitic carbon, the interplanar spacing of 0.34 nm corresponds to its (002) plane (Graphite-2H, PDF# 41-1487). The clear and ordered lattice fringes indicate a high degree of graphitization even after ball milling. The HRTEM images of Fig. 4d, e and f clearly indicate the lattice fringes of Si and Fe_3O_4. The interplanar spacings of 0.48 and 0.25 nm correspond to (111) and (311) planes of Fe_3O_4 (Fe_3O_4, PDF#89-0688), and the interplanar spacing of 0.31 nm corresponds to the (111) plane of crystalline Si (Si, PDF#77-2108). This intuitively proves that Fe_3O_4 nanocrystals with a particle size of 5~10 nm were successfully synthesized with a good combination of Si and graphite sheets.

The EDS mapping results in Fig. 4g, h show the integrated structure of Si, C, and Fe_3O_4. It is worth noting that the component of Si and Fe_3O_4 still show uniform distribution after 20 min of ultrasonic dispersion. The fine Fe_3O_4 particles surround Si like a mist, which not only boosts the conductivity of Si nanoparticles, but also helps to more tightly connect Si and graphite sheet matrix. It is believed

that such a good interfacial configuration can alleviate the volume expansion of Si during the repeat lithiation/delithiation process, enhance the electronic conductivity and structural stability of the silicon/carbon anode. In addition, the elemental mapping of Cr and Mn appears because ball mill beads of 201 stainless steel contains Mn and Cr elements, which is consistent with the XPS full spectrum data in Fig. 3.

A standard coin-type half-cell was assembled for evaluating the electrochemical performance of Si@Fe_3O_4@C, Si@C and pure Si electrodes. The initial five cycles of cyclic voltammetry (CV) curves of Si@Fe_3O_4@C at a scan rate of 0.01 mV s^{-1} are shown in Fig. 5a. During the first lithiation process, a broad reduction peak appears at 0.70 V, which is mainly attributed to the formation of SEI film and irreversible reactions, and disappear in subsequent cycles. Another reduction peak around 0.01 V corresponds to the alloying of crystalline Si to form a series of Li_xSi alloys ($0 \le x \le 3.75$) and the intercalation of Li ions into graphite sheets.[38] In the
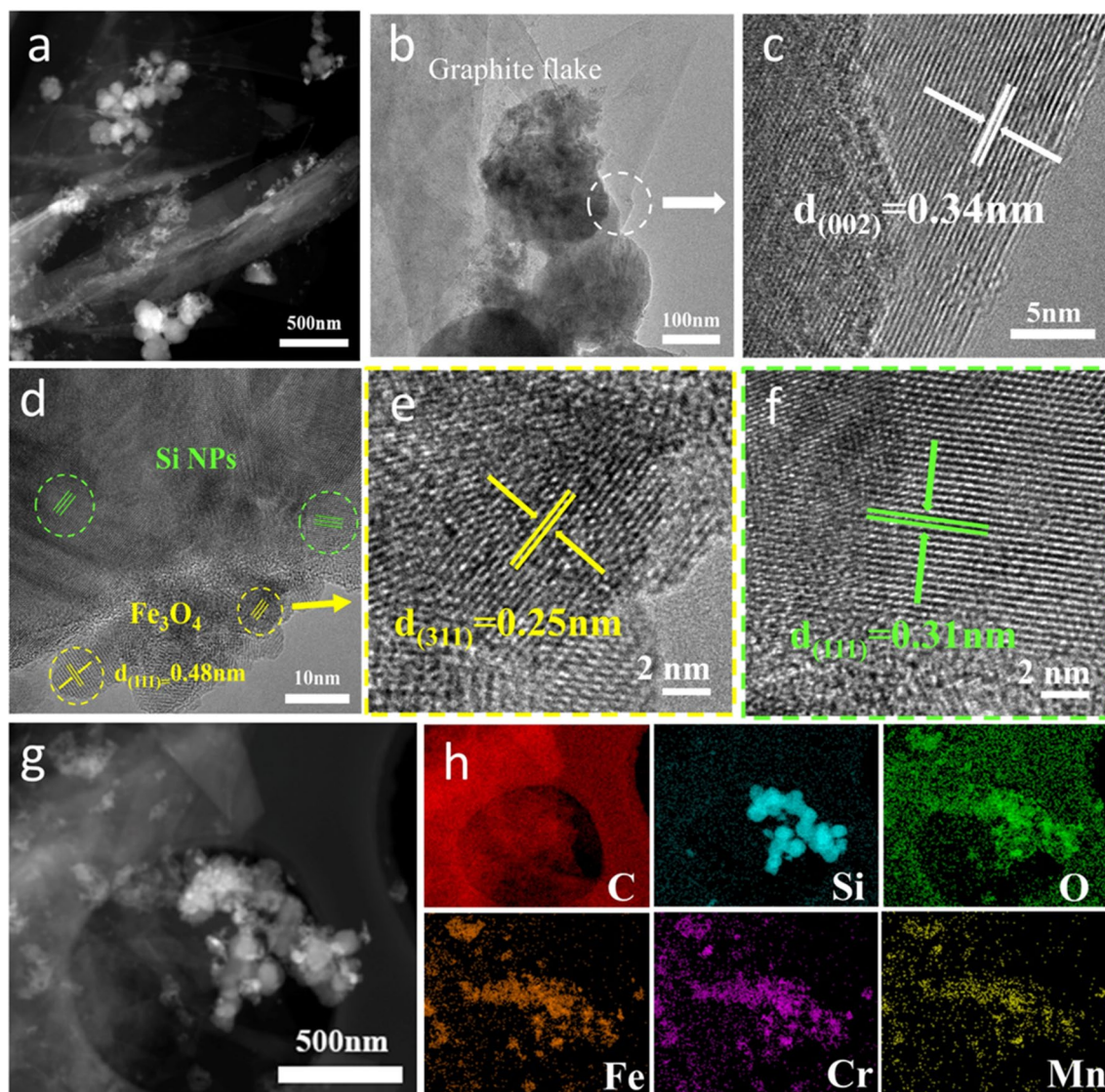
Fig. 4 (a–b) TEM and (c–f) HRTEM images of Si@Fe$_3$O$_4$@C, (g–h) STEM image and the corresponding EDS mapping of C, Si, O, Fe, Cr and Mn for Si@Fe$_3$O$_4$@C before cycling.

subsequent de-lithiation process, multiple oxidation peaks at 0.16 V, 0.33 V, and 0.49 V can be observed. The peak at 0.16 V represents the extraction of lithium ions from the graphite sheet, while the peaks at 0.33 V and 0.49 V demonstrate the multi-step dealloying process of the transformation from Li$_x$Si alloys to amorphous silicon, respectively. Afterwards, the peak potential and shape of the CV curves show a little change. Because of the transformation of crystalline state into amorphous Si, and the corresponding alloying reaction of amorphous Si and Li occurs around 0.21 V.[39] In addition, a steamed bread reduction peak at 0.86 V paired with a broad oxidation peak at 1.5 V~2 V are seen from CVs. The highly coincidence reveals a good reversibility for lithiation/ de-lithiation process of Fe$_3$O$_4$ (Fe$_3$O$_4$ + Li $\rightleftarrows$ Fe + Li$_2$O).[26] Furthermore, the redox peak intensity of Si increases with

the cycle number as a result of electrode activation. Figure 5b shows the charge–discharge curves of Si@Fe$_3$O$_4$@C at a current density of 0.2 A g^{-1} in the voltage range of 0.01~3 V. The initial discharge and charge capacities are 1115 and 815 mA h g^{-1}, respectively. The first coulombic efficiency (CE) is calculated as 73%, and afterwards, stabilizes at 97~99% in the subsequent cycles.

Figure 5c compares the cycling performance of MCMB, Si, Si@Fe$_3$O$_4$@C and Si@C. As expected, MCMB exhibits typical graphite anode characteristics with good reversibility and cycling stability, its reversible capacity is about 380 mA h g^{-1} upon cycling. The Si anode has a high initial capacity of 3418 mA h g^{-1}, but suffers a rapid decay to 669 mA h g^{-1} after 110 cycles with a low capacity retention of 19.5%. For the Si@C composite, the initial capacity decay
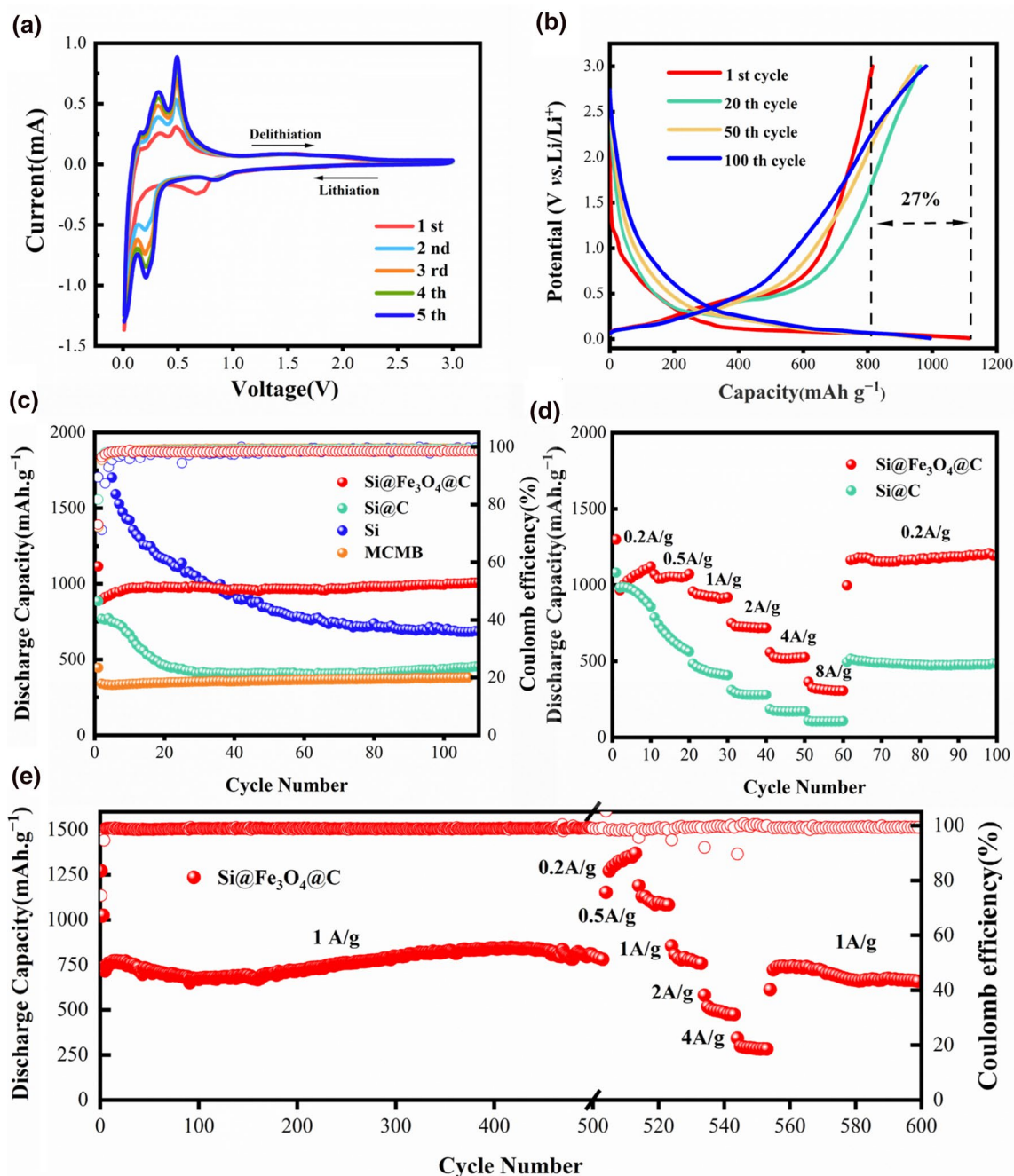
Fig. 5 (a) CV curves of Si@Fe$_3$O$_4$@C at the initial 5 cycles; (b) Charge-discharge curves of Si@Fe$_3$O$_4$@C at 0.2 A g^{-1}; (c) Cycling performance at 0.2 A g^{-1}; (d) Rate capability at different current densities; (e) Long cycle performance and rate performance of Si@Fe$_3$O$_4$@C at a current density of 1 A g^{-1} after 500 cycles.

is also quick, but after 20 cycles, it is stabilized at 460 mA h g^{-1}. Indicating that MCMB can improve the cycling stability of Si to some extent. Compared with the Si@C composite, Si@Fe$_3$O$_4$@C exhibits much improved cycling stability than Si, which is comparable to commercial MCMB anode. Thus, it is inferred that Fe$_3$O$_4$ could well stabilize the silicon-carbon interface and accommodate great volume change of Si

particles during cycling, which is further reflected by the cycling performance at 1 A g^{-1}. As shown in Fig. 5e, the capacity of the Si@Fe$_3$O$_4$@C composite is basically stable at 780 mA h g^{-1} within 500 cycles. Then, the electrode was continued to be cycled at various current densities of 0.2 A g^{-1}, 0.5 A g^{-1}, 1.0 A g^{-1}, 2.0 A g^{-1} and 4.0 A g^{-1}. When recovering to 1 A g^{-1}, it still shows a specific capacity of

723 mA h g^{-1}. As compared to Si@C, the Si@Fe$_3$O$_4$@C composite exhibits excellent rate capability in Fig. 5d. When cycled at different current densities of 0.2 A g^{-1}, 0.5 A g^{-1}, 1 A g^{-1}, 2 A g^{-1}, 4 A g^{-1} and 8 A g^{-1}, the Si@Fe$_3$O$_4$@C anode can provide capacities of 1122 mA h g^{-1}, 1073 mA h g^{-1}, 919 mA h g^{-1}, 718 mA h g^{-1}, 525 mA h g^{-1} and 306 mA h g^{-1}, respectively. After such a severe cycling shock, when the current density is restored to 0.2 A g^{-1}, it still maintains capacity of 1216 mA h g^{-1} for 40 cycles, and shows no obvious capacity fading. It indicates that the introduction of Fe$_3$O$_4$ can improve the rate capability of the composites.

To gain a deep understanding of the role of Fe$_3$O$_4$ in the electrochemical reaction, The charge and discharge voltage is controlled in the range of 0 V~1.5 V to suppress the Li$^+$ extraction of Fe$_3$O$_4$ during cycling. As shown in the CV curves of Figure S4a, the Si@Fe$_3$O$_4$@C composite exhibits the Li$^+$ extraction/insertion process of pure Si/C at 0.01 V~1.5 V. During the subsequent cycles, without the participation of Fe$_3$O$_4$, the composite loses its excellent cycling stability, and the capacity decays to 585 mA h g^{-1} after 100 cycles (Figure S4b). This indicates that Fe$_3$O$_4$ nanoparticles improve the cycling stability when the composite was cycled in the voltage range of 0.01 V~3.0 V.

To further understand excellent electrochemical performance of Si@Fe$_3$O$_4$@C, EIS were investigated to evaluate the electrical conductivity of electrode/electrolyte interfaces. Before cycling, all EIS present one semicircle in the high-frequency region and a sloping line in the medium-low region, which could be attributed to the charge-transfer resistance at the electrode/electrolyte interface (R_{ct}) and the Warburg impedance in the bulk electrode (Z_w).[40,41] As

shown in Fig. 6, the R_{ct} value of the Si@Fe$_3$O$_4$@C (51 Ω) is significantly smaller than that of pure Si electrode (298 Ω), which indicates that the composite can provide a faster electron transfer channel and its electrical conductivity is significantly improved. After cycling, two semicircles appear in the Nyquist plots, the first semicircle corresponds to the SEI layer resistance (R_f), while the second semicircle corresponds to the charge transfer resistance. After 600 cycles, the R_{ct} of Si@Fe$_3$O$_4$@C decreases to 32 Ω. One reason is that the electrical conductivity is increased by Li$^+$ embedding. Another reason is that the iron derived from electrochemical reaction could effectively improve the conductivity of electrode.

In order to explore the morphology changes of the electrode during the charge-discharge cycles, Fig. 7 presents the SEM images of bare Si and Si@Fe$_3$O$_4$@C electrodes before and after 600 cycles. Apparently, the surface morphology of the bare Si and Si@Fe$_3$O$_4$@C shows great difference after long-term cycling, the bare Si electrode is chapped, and the active materials lose close contact. Observed under a high-magnification SEM, the original Si particles have been crushed and broken (Fig. 7c). In contrast, the Si@Fe$_3$O$_4$@C electrode still keeps good contact and no obvious cracks appear on the electrode surface. In addition, Fig. 7f shows that Si@Fe$_3$O$_4$@C maintains the complete Si particle morphology, and the surface of the Si particles is wrapped with SEI films, which explains the good cycling stability of Si@Fe$_3$O$_4$@C from a structural point of view. The EDS mapping regions of each element show high consistency (Fig. 7g), indicating that the combination of Si, C and Fe becomes more and more tight during cycling, which helps to maintain the complete structure of Si particles.
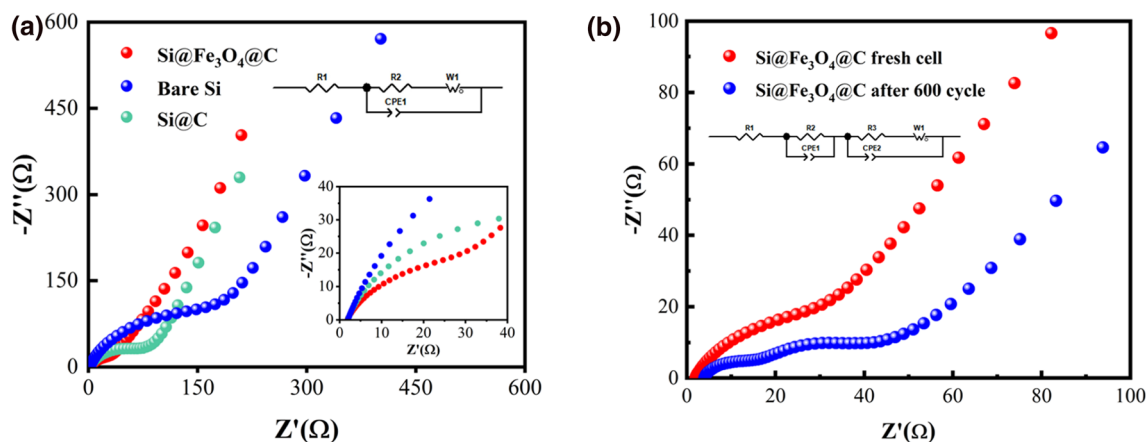

Fig. 6 (a) Nyquist plots and the equivalent circuit model inset of the Si@Fe$_3$O$_4$@C, bare Si and Si@C before cycling; (b) Nyquist plots and the equivalent circuit model inset of the Si@Fe$_3$O$_4$@C after 600 cycles.
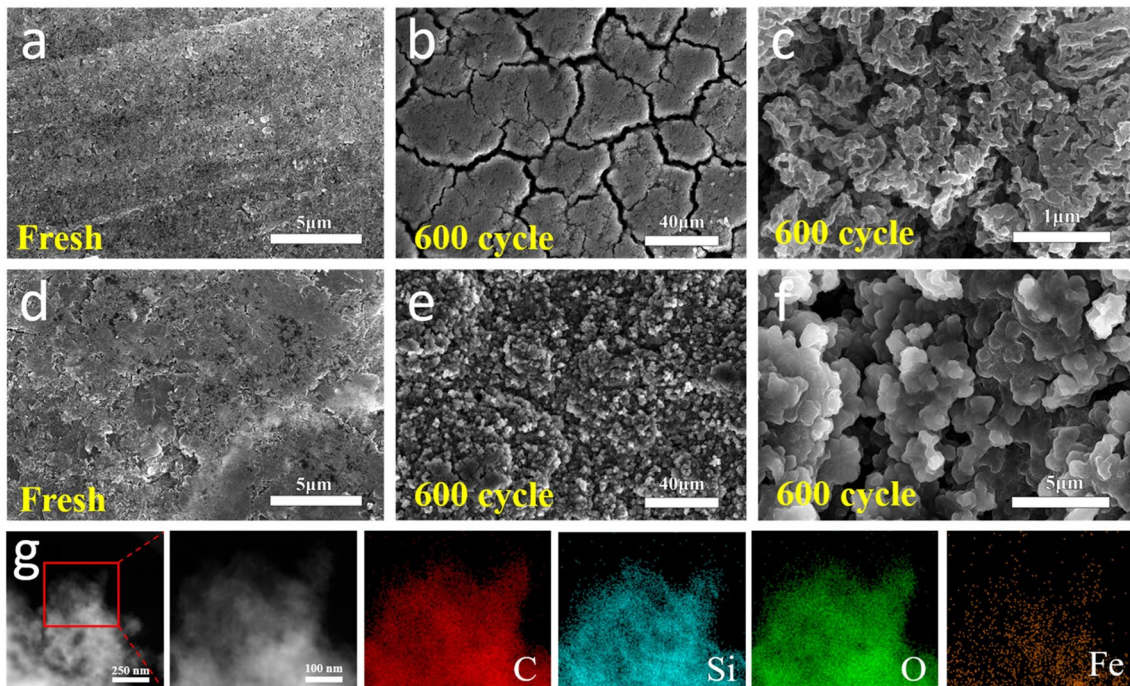
Fig. 7 (a–c) SEM image of bare Si after 600 cycles at 1 A g^{-1}; (d–f) SEM image of Si@Fe$_3$O$_4$@C after 600 cycles at 1 A g^{-1}; (g) EDS mapping images of the corresponding element after cycling.

Conclusions

In summary, a Si@Fe$_3$O$_4$@C composite was successfully prepared by a facile, ball-milling route combined with subsequent heating treatment. Si and Fe$_3$O$_4$ nanoparticles were tightly contacted with the as-milled graphite sheet from MCMB. Fe$_3$O$_4$ not only provides some of the capacity, but also plays a role in stabilizing the SEI film. As a result, the Si@Fe$_3$O$_4$@C composite shows much improved lithium storage properties than Si/C, The Si@Fe$_3$O$_4$@C composite reveals a reversible capacity of 1009 mA h g^{-1} at 200 mA g^{-1} after 110 cycles and 780.8 mA h g^{-1} at 1 A g^{-1} after 500 cycles, presenting excellent cycling stability and rating performance as LIBs anode. In other words, this research puts forward a scalable and effective method for the industrial production of high-capacity Si-based anodes for LIBs.

References

1. F. Zhou, X.S. Yang, J. Liu, J. Liu, R. Hu, L. Ouyang, and M. Zhu, In-Situ Introducing TiP$_2$ Nanocrystals in Black Phosphorus Anode to Promote High Rate-Capacity Synergy. *J. Power Sources* 499, 229979 (2021).
2. Z. Zheng, H.H. Wu, H. Liu, Q. Zhang, X. He, S. Yu, V. Petrova, J. Feng, R. Kostecki, P. Liu, D.L. Peng, M. Liu, and M.S. Wang, Achieving Fast and Durable Lithium Storage through Amorphous FeP Nanoparticles Encapsulated in Ultrathin 3D P-Doped Porous Carbon Nanosheets. *ACS Nano* 14, 9545 (2020).
3. S.D.A. Zaidi, C. Wang, B. György, C. Sun, H. Yuan, L. Tian, and J. Chen, Iron and Silicon Oxide Doped/PAN-Based Carbon Nanofibers as Free-Standing Anode Material for Li-ion Batteries. *J. Colloid Interface Sci.* 569, 164 (2020).
4. Q. Zhao, X. Chen, W. Hou, B. Ye, Y. Zhang, X. Xia, and J. Wang, A Facile, Scalable, High Stability Lithium Metal Anode. *SusMat* 2, 104 (2022).
5. Z. Xiao, C. Lei, C. Yu, X. Chen, Z. Zhu, H. Jiang, and F. Wei, Si@Si$_3$N$_4$@C Composite with Egg-Like Structure as High-Performance Anode Material for Lithium ion Batteries. *Energy Storage Mater.* 24, 565 (2020).
6. Y. Li, W. Liu, Z. Long, P. Xu, Y. Sun, X. Zhang, S. Ma, and N. Jiang, Si@C Microsphere Composite with Multiple Buffer Structures for High-Performance Lithium-Ion Battery Anodes. *Chem. Eur. J.* 24, 12912 (2018).
7. H. Wang, H. Man, J. Yang, J. Zang, R. Che, F. Wang, D. Sun, and F. Fang, Self-Adapting Electrochemical Grinding Strategy for Stable Silicon Anode. *Adv. Funct. Mater.* 32, 2109887 (2021).
8. Y. He, L. Jiang, T. Chen, Y. Xu, H. Jia, R. Yi, D. Xue, M. Song, A. Genc, C. Bouchet-Marquis, L. Pullan, T. Tessner, J. Yoo, X.

Li, J.G. Zhang, S. Zhang, and C. Wang, Progressive Growth of the Solid-Electrolyte Interphase Towards the Si Anode Interior Causes Capacity Fading. *Nanomater. Nanotechnol.* 16, 1113 (2021).

9. R. Fang, R. Li, Z. Wang, C. Miao, W. Xiao, Y. Zhang, X. Yan, and Y. Jiang, Novel High-Performance Si-SiO₂@Fe/C Composite Anodes from Low-Cost and Industrial AlSiFe Alloy Powders. *Solid State Ion* 337, 42 (2019).

10. X. Gao, W. Lu, and J. Xu, Insights into the Li Diffusion Mechanism in Si/C Composite Anodes for Lithium-Ion Batteries. *ACS Appl. Mater. Interfaces* 13, 21362 (2021).

11. M. Chen, W. Cao, L. Wang, X. Ma, and K. Han, Chessboard-Like Silicon/Graphite Anodes with High Cycling Stability toward Practical Lithium-Ion Batteries. *ACS Appl. Energy Mater.* 4, 775 (2020).

12. W. Luo, C. Fang, X. Zhang, J. Liu, H. Ma, G. Zhang, Z. Liu, and X. Li, In Situ Generated Carbon Nanosheet-Covered Micron-Sized Porous Si Composite for Long-Cycling Life Lithium-Ion Batteries. *ACS Appl. Energy Mater.* 4, 535 (2020).

13. P. Li, H. Kim, S.T. Myung, and Y.-K. Sun, Diverting Exploration of Silicon Anode into Practical Way: A Review Focused on Silicon-Graphite Composite for Lithium Ion Batteries. *Energy Storage Mater.* 35, 550 (2021).

14. D. Sui, Y. Xie, W. Zhao, H. Zhang, Y. Zhou, X. Qin, Y. Ma, Y. Yang, and Y. Chen, A High-Performance Ternary Si Composite Anode Material with Crystal Graphite Core and Amorphous Carbon Shell. *J. Power Sources* 384, 328 (2018).

15. X. Shen, Z. Tian, R. Fan, L. Shao, D. Zhang, G. Cao, L. Kou, and Y. Bai, Research Progress on Silicon/Carbon Composite Anode Materials for Lithium-Ion Battery. *J. Energy Chem.* 27, 1067 (2018).

16. F. Dou, L. Shi, G. Chen, and D. Zhang, Silicon/Carbon Composite Anode Materials for Lithium-Ion Batteries. *Electrochem. Energy Rev.* 2, 149 (2019).

17. X. Shan, Y. Zhong, L. Zhang, Y. Zhang, X. Xia, X. Wang, and J. Tu, A Brief Review on Solid Electrolyte Interphase Composition Characterization Technology for Lithium Metal Batteries: Challenges and Perspectives. *J. Phys. Chem. C* 125, 19060 (2021).

18. C. Wang, Y. Li, F. Cao, Y. Zhang, X. Xia, and L. Zhang, Employing Ni-Embedded Porous Graphitic Carbon Fibers for High-Efficiency Lithium-Sulfur Batterie. *ACS Appl. Mater. Interfaces* 14, 10457 (2022).

19. Y. Xia, T. Zhao, X. Zhu, Y. Zhao, H. He, C.T. Hung, X. Zhang, Y. Chen, X. Tang, J. Wang, W. Li, and D. Zhao, Inorganic-Organic Competitive Coating Strategy Derived Uniform Hollow Gradient-Structured Ferroferric Oxide-Carbon Nanospheres for Ultra-Fast and Long-Term Lithium-Ion Battery. *Nat. Commun.* 12, 2973 (2021).

20. B.H. Hou, Y.Y. Wang, J.Z. Guo, Y. Zhang, Q.L. Ning, Y. Yang, W.H. Li, J.P. Zhang, X.L. Wang, and X.L. Wu, A Scalable Strategy To Develop Advanced Anode for Sodium-Ion Batteries: Commercial Fe₃O₄-Derived Fe₃O₄@FeS with Superior Full-Cell Performance. *ACS Appl. Mater. Interfaces* 10, 3581 (2018).

21. J. Jang, S.H. Song, H. Kim, J. Moon, H. Ahn, K.I. Jo, J. Bang, H. Kim, and J. Koo, Janus Graphene Oxide Sheets with Fe₃O₄ Nanoparticles and Polydopamine as Anodes for Lithium-Ion Batteries. *ACS Appl. Mater. Interfaces* 13, 14786 (2021).

22. C. Han, L. Xu, H. Li, R. Shi, T. Zhang, J. Li, C.P. Wong, F. Kang, Z. Lin, and B. Li, Biopolymer-Assisted Synthesis of 3D Interconnected Fe₃O₄@Carbon Core@Shell as Anode for Asymmetric Lithium Ion Capacitors. *Carbon* 140, 296 (2018).

23. Q. Wang, C. Guo, J. He, S. Yang, Z. Liu, and Q. Wang, Fe₂O₃/C-Modified Si Nanoparticles as Anode Material for High-Performance Lithium-Ion Batteries. *J. Alloys Compd.* 795, 284 (2019).

24. Y. Yan, Y. Chen, Y. Li, X. Wu, C. Jin, and Z. Wang, Synthesis of Si/Fe₂O₃-Anchored rGO Frameworks as High-Performance Anodes for Li-Ion Batteries. *Int. J. Mol. Med.* 22, 11041 (2021).

25. G. Grinbom, D. Duveau, G. Gershinsky, L. Monconduit, and D. Zitoun, Silicon/Hollow γ-Fe₂O₃ Nanoparticles as Efficient Anodes for Li-Ion Batteries. *Chem. Mater.* 27, 2703 (2015).

26. C. Liao, and S. Wu, Pseudocapacitance Behavior on Fe₃O₄-Pillared SiOₓ Microsphere Wrapped by Graphene as High Performance Anodes for Lithium-Ion Batteries. *Chem. Eng. J.* 355, 805 (2019).

27. L. Su, Y. Zhong, and Z. Zhou, Role of Transition metal Nanoparticles in the Extra Lithium Storage Capacity of Transition Metal Oxides: A Case Study of Hierarchical Core–Shell Fe 3 O 4@ C and Fe@ C Microspheres. *J. Mater. Chem. A* 1, 15158–15166 (2013).

28. C. Liu, Q. Xia, C. Liao, and S. Wu, Pseudocapacitance Contribution to Three-Dimensional Micro-Sized Silicon@Fe₃O₄@Few-Layered Graphene for High-Rate and Long-Life Lithium Ion Batteries. *Mater. Today Commun.* 18, 66 (2019).

29. H. Wang, Y. Ding, J. Nong, Q. Pan, Z. Qiu, X. Zhang, F. Zheng, Q. Wu, Y. Huang, and Q. Li, Bifunctional NaCl Template for the Synthesis of Si@Graphitic Carbon Nanosheets as Advanced Anode Materials for Lithium Ion Batteries. *New J. Chem.* 44, 14278 (2020).

30. Q. He, M. Ashuri, Y. Liu, B. Liu, and L. Shaw, Silicon Microreactor as a Fast Charge, Long Cycle Life Anode with High Initial Coulombic Efficiency Synthesized via a Scalable Method. *ACS Appl. Energy Mater.* 4, 4744 (2021).

31. J. Han, X. Tang, S. Ge, Y. Shi, C. Zhang, F. Li, and S. Bai, Si/C Particles on Graphene Sheet as Stable Anode for Lithium-Ion Batteries. *J. Mater. Sci. Technol.* 80, 259 (2021).

32. H. Huang, G. Yang, J. Yu, J. Zhang, Y. Xia, K. Wang, C. Liang, Y. Gan, X. He, and W. Zhang, One-Pot Synthesis of Nanocrystalline SnS@ Tremella-Like Porous Carbon by Supercritical CO₂ Method for Excellent Sodium Storage Performance. *Electrochim. Acta* 373, 137933 (2021).

33. J. Chen, Z. Mao, L. Zhang, D. Wang, R. Xu, L. Bie, and B.D. Fahlman, Nitrogen-Deficient Graphitic Carbon Nitride with Enhanced Performance for Lithium Ion Battery Anodes. *ACS Nano* 11, 12650 (2017).

34. L. Shi, W. Wang, A. Wang, K. Yuan, Z. Jin, and Y. Yang, Scalable Synthesis of Core-Shell Structured SiO x/Nitrogen-Doped Carbon Composite as a High-Performance Anode Material for Lithium-Ion Batteries. *J. Power Sources* 318, 184 (2016).

35. N. Zhang, C. Chen, X. Yan, Y. Huang, J. Li, J. Ma, and D.H.L. Ng, Bacteria-Inspired Fabrication of Fe₃O₄-Carbon/Graphene Foam for Lithium-Ion Battery Anodes. *Electrochim. Acta* 223, 39 (2017).

36. P. Sabhapathy, C.C. Liao, W.F. Chen, T.C. Chou, I. Shown, A. Sabbah, Y.G. Lin, J.F. Lee, M.K. Tsai, K.H. Chen, and L.C. Chen, Highly Efficient Nitrogen and Carbon Coordinated N-Co-C Electrocatalysts on Reduced Graphene Oxide Derived from Vitamin-B12 for the Hydrogen Evolution Reaction. *J. Mater. Chem. A* 7, 7179 (2019).

37. W. Ren, H. Zhang, C. Guan, and C. Cheng, Ultrathin MoS₂ Nanosheets@Metal Organic Framework-Derived N-Doped Carbon Nanowall Arrays as Sodium Ion Battery Anode with Superior Cycling Life and Rate Capability. *Adv. Funct. Mater.* 27, 1702116 (2017).

38. P. Limthongkul, Y.I. Jang, N.J. Dudney, and Y.M. Chiang, Electrochemically-Driven Solid-State Amorphization in Lithium-Silicon Alloys and Implications for Lithium Storage. *Acta Mater.* 51, 1103 (2003).

39. M. Furquan, A.R. Khatribail, S. Vijayalakshmi, and S. Mitra, Efficient Conversion of Sand to Nano-Silicon and its Energetic Si-C

Composite Anode Design for High Volumetric Capacity Lithium-Ion Battery. *J. Power Sources* 382, 56–68 (2018).

40. X. Pu, M. Liu, L. Li, C. Zhang, Y. Pang, C. Jiang, L. Shao, W. Hu, and Z.L. Wang, Efficient Charging of Li-Ion Batteries with Pulsed Output Current of Triboelectric Nanogenerators. *Adv. Sci. (Weinh)* 3, 1500255 (2016).

41. M. Zhang, Y. Li, E. Uchaker, S. Candelaria, L. Shen, T. Wang, and G. Cao, Homogenous Incorporation of SnO_2 Nanoparticles in Carbon Cryogels via the Thermal Decomposition of Stannous Sulfate and their Enhanced Lithium-Ion Intercalation Properties. *Nano Energy* 2, 769 (2013).